

Flexible Intelligent Metasurfaces in High-Mobility MIMO Integrated Sensing and Communications

Kuranage Roche Rayan Ranasinghe[✉], *Graduate Student Member, IEEE*, Jiancheng An[✉], *Member, IEEE*, Iván Alexander Morales Sandoval[✉], *Graduate Student Member, IEEE*, Hyeon Seok Rou[✉], *Member, IEEE*, Giuseppe Thadeu Freitas de Abreu[✉], *Senior Member, IEEE*, Chau Yuen[✉], *Fellow, IEEE*, and Mérouane Debbah[✉], *Fellow, IEEE*

Abstract—We propose a novel doubly-dispersive (DD) multiple-input multiple-output (MIMO) channel model incorporating flexible intelligent metasurfaces (FIMs), which is suitable for integrated sensing and communications (ISAC) in high-mobility scenarios. We then discuss how the proposed FIM-parameterized DD (FPDD) channel model can be applied in a logical manner to ISAC waveforms that are known to perform well in DD environments, namely, orthogonal frequency division multiplexing (OFDM), orthogonal time frequency space (OTFS), and affine frequency division multiplexing (AFDM). Leveraging the proposed model, we formulate an achievable rate maximization problem with a strong sensing constraint for all the aforementioned waveforms, which we then solve via a gradient ascent algorithm with closed-form gradients presented as a bonus. Our numerical results indicate that the achievable rate is significantly impacted by the emerging FIM technology with careful parametrization essential in obtaining strong ISAC performance across all waveforms suitable to mitigating the effects of DD channels.

Index Terms—Doubly-dispersive channel, Achievable Rate, MIMO, FIM, OFDM, OTFS, AFDM, ISAC, B5G, 6G.

I. INTRODUCTION

NEXT-generation wireless networks in the beyond fifth generation (B5G) and sixth generation (6G) are expected to meet unprecedented performance demands and support a diverse range of applications, such as integrated sensing and communications (ISAC) [1], integrated communication and computing (ICC) [2], [3], virtual reality (VR)/extended reality (XR) [4], intelligent traffic networks (ITN) [5], space-air-ground integrated network (SAGIN) [6], holographic communications [7], and massive internet of things (IoT) [8], [9].

As expected above, 6G networks will increasingly operate in challenging wireless channels, i.e., in high-mobility multipath applications such as vehicle-to-everything (V2X), high-speed rail, unmanned aerial vehicle (UAV), low-earth orbit (LEO) satellite, and SAGIN links which involve nodes moving at significant velocities [10]. Such environments are well-known to exhibit channel responses that are both time-selective and

frequency-selective (often described as time-frequency selective fading, or doubly-dispersive channels), which incorporate both the temporal variation (Doppler shifts) and frequency dispersion (multipath delays) [11]. Therefore, modeling beyond the quasi-static or frequency-flat assumptions commonly used in conventional wireless communication system models are essential to accurately capture the propagation effects in these scenarios [12], [13].

Notably, the inherent delay-Doppler structure of such channels can be leveraged for communication robustness and for ISAC [14], [15] - for example, enabling radar parameter estimation (e.g., target range and velocity) directly from communication waveforms [16]–[19]. This opens the door to native and efficient *communication-centric* ISAC techniques that unify data transmission and environmental sensing within the same infrastructure [20], highlighting the need for the development of models capable of leveraging these properties.

On the other hand, instead of channel modeling, another very promising approach to achieve robustness and control over the challenging wireless channel is to directly manipulate the propagation environment itself using reconfigurable electromagnetic structures, which has been attracting great attention in the recent years [21]–[24]. The most standard and widely-investigated example is the reconfigurable intelligent surface (RIS) – which are planar metasurfaces with tunable meta-atom elements – having been extensively studied as a means to engineer reflections and enhance wireless coverage and capacity in an energy-efficient manner [25]–[28]. More recently, enhanced metasurface architectures such as stacked intelligent metasurfaces (SIM) have been developed to perform elaborate signal processing directly in the electromagnetic wave domain [29], [30], which comprises a large number of tunable meta-atoms collected into layers and *stacked* very close to one another.

Building upon these advances, an emerging paradigm is the *flexible* variant, known as the flexible intelligent metasurface (FIM), a metasurface that can physically reconfigure or morph its three-dimensional (3D) surface shape in response to time-varying wireless channel conditions [31]–[34]. Unlike traditional RISs that rely solely on electronically controlled phase shifts, FIMs can adjust the positions of their meta-atoms in the normal direction of the planar surface. This synergistic combination of physical and electronic flexibility provides FIMs with enhanced spatiotemporal control capabilities that exceed those of conventional RISs with static structures [35]. For instance, Ni *et al.* [36] have developed a reconfigurable FIM

K. R. R. Ranasinghe, I. A. M. Sandoval, H. S. Rou and G. T. F. de Abreu are with the School of Computer Science and Engineering, Constructor University (previously Jacobs University Bremen), Campus Ring 1, 28759 Bremen, Germany (emails: {kranasinghe, imorales, hrou, gabreu}@constructor.university).

J. An and C. Yuen is with the School of Electrical and Electronics Engineering, Nanyang Technological University, Singapore 639798 (e-mails: {jiancheng.an, chau.yuen}@ntu.edu.sg).

M. Debbah is with the KU 6G Research Center, Department of Computer and Information Engineering, Khalifa University, Abu Dhabi, United Arab Emirates, and also with the CentraleSupélec, University Paris-Saclay, 91192 Gif-sur-Yvette, France (e-mail: merouane.debbah@ku.ac.ae).

that uses a liquid metal soft microfluidic network embedded within an elastomeric matrix, controlled by electromagnetic actuation. This innovative design allows for real-time and programmable surface shape morphing with fully reversible properties. More recently, another innovative FIM was constructed using an array of tiny metallic filaments [32], actuated by reprogrammable distributed Lorentz forces generated by electrical currents passing through a static magnetic field. This setup grants the FIM precise and rapid dynamic morphing capabilities, enabling it to promptly altering its structure¹. Additionally, incorporating a mechanical locking mechanism can sustain the newly morphed shapes.

Recent groundbreaking research has unveiled the considerable benefits of FIM technology in wireless communication and sensing systems [37], [38]. In [37], An *et al.* explored the function of FIMs as multiple-input multiple-output (MIMO) transceiver arrays. They characterized the capacity limits of FIM-aided MIMO transmissions over frequency-flat fading channels by jointly optimizing the 3D surface shape configurations of both transmitting and receiving FIMs, as well as the transmit covariance matrix. The numerical results demonstrated that FIMs can double the MIMO capacity compared to conventional rigid arrays under specific system settings. Furthermore, they investigated FIM-assisted multiuser downlink communications [31], focusing on minimizing the transmit power at the base station (BS) by jointly optimizing transmit beamforming and the FIM surface configuration, while meeting the quality of service (QoS) requirements for all users and adhering to the maximum morphing range of the FIM. Indeed, simulation results showed that the FIM can reduce the required transmit power by nearly 3 dB compared to conventional rigid two-dimensional (2D) arrays, while maintaining the same data rate. More recently, Teng *et al.* [38] examined the impact of FIM on wireless sensing performance under the per-antenna power constraint. Their findings indicated that the cumulated power of the probing signals at target locations was improved by 3 dB by optimizing the surface shape of the transmitting FIM.

However, to fully harness FIMs in high-mobility and MIMO ISAC contexts, it is crucial to integrate their functionality with appropriate channel models and system design frameworks. Many existing studies on intelligent metasurfaces assume simplified channel conditions (e.g., static or block-fading channels and frequency-flat propagation), which may not hold in fast-varying environments. Therefore, the joint consideration of metasurface reconfigurability and doubly-dispersive channel behavior is largely uncharted, albeit essential for realizing the full potential of metasurfaces in practical scenarios.

A recent effort by Ranasinghe *et al.* [39], [40] took a step in this direction by formulating a parametric doubly-dispersive (DD) channel model that includes metasurface-based transceivers (SIMs at the transmitter and receiver) and intermediate RIS panels in the environment, which demonstrated how metasurface parameters can be incorporated into the delay-Doppler domain channel characterization, allowing

the design of waveforms (such as orthogonal frequency division multiplexing (OFDM), orthogonal time frequency space (OTFS) and affine frequency division multiplexing (AFDM)) and transceiver strategies tailored to time-varying multipath conditions, with a corresponding ISAC analysis done in [41].

However, the paradigm of flexible metasurfaces introduces additional challenges and opportunities that remain open. In particular, the physical shape-shifting capability of FIMs add a new layer of complexity to channel modeling and optimization, as the channel response itself can be altered in real time by the metasurface geometry. Therefore in this article, we explore the integration of FIM technology with doubly-dispersive channel modeling for the B5G/6G MIMO ISAC paradigm.

The contributions of this paper are summarized as follows:

- We describe a novel FIM-parameterized DD (FPDD) channel model which can be applied to the design of ISAC waveforms known to perform well in DD environments, such as OFDM, OTFS, and AFDM, as well as to derive their complete input-output (I/O) relationships in the corresponding domains.
- We formulate and solve – via a gradient ascent algorithm with corresponding closed-form gradients – an achievable rate maximization problem with a strong sensing constraint for all the aforementioned waveforms and under the given model. We highlight that both the model and the optimization problem are contributions on their own.
- Simulation results indicate that the achievable rate is significantly impacted by the emerging FIM technology with careful parametrization essential in obtaining strong ISAC performance across all waveforms suitable to mitigating the effects of DD channels.

Notation: All scalars are represented by upper or lowercase letters, while column vectors and matrices are denoted by bold lowercase and uppercase letters, respectively. The diagonal matrix constructed from vector \mathbf{a} is denoted by $\text{diag}(\mathbf{a})$, while \mathbf{A}^T , \mathbf{A}^H , $\mathbf{A}^{1/2}$, and $[\mathbf{A}]_{i,j}$ denote the transpose, Hermitian, square root and the (i,j) -th element of a matrix \mathbf{A} , respectively. The convolution and Kronecker product are respectively denoted by $*$ and \otimes , while \mathbf{I}_N and \mathbf{F}_N represent the $N \times N$ identity and the normalized N -point discrete Fourier transform (DFT) matrices, respectively. The sinc function is expressed as $\text{sinc}(a) \triangleq \frac{\sin(\pi a)}{\pi a}$, and $j \triangleq \sqrt{-1}$ denotes the elementary complex number.

II. THE PROPOSED FIM MIMO CHANNEL MODEL

A. FIM Antenna Array Response

Let $\theta \in [0, \pi]$ and $\phi \in [-\frac{\pi}{2}, \frac{\pi}{2}]$ denote the arbitrary angle-of-arrival (AoA) or angle-of-departure (AoD) elevation and azimuth angles [42], [43] of a channel propagation path to (or from) a flexible uniform planar array (UPA) with $B \triangleq B_x B_z$ elements², where B_x and B_z refer to the number of antenna elements along the x -axis and y -axis, respectively, with $\mathcal{B} \triangleq \{1, 2, \dots, B\}$ denoting the set of antenna elements.

²Without loss of generality, the UPA is aligned parallel to the y direction with elements occupying space in the x and z dimensions. The generalization to arbitrary axes is trivial; some other orientations are discussed in [44].

¹A video showing the real-time morphing ability of an FIM can be found at <https://www.eurekalert.org/multimedia/950133>.

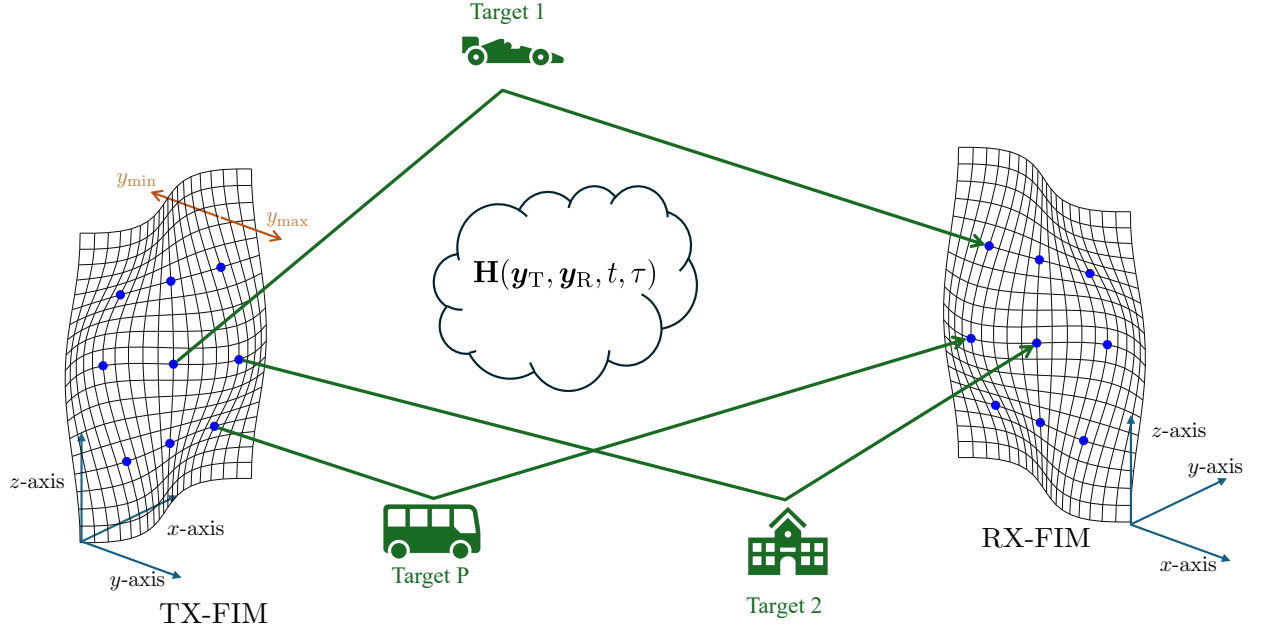


Fig. 1: The considered FIM MIMO system for high-mobility scenarios, which includes two FIMs, one acting as the transmitter (TX) and the other as the receiver (RX), with 3 scatterers of interest.

The key principle of a FIM stems from the fact that each radiating element is allowed some movement in an additional third dimension; *i.e.*, the y -axis via a connected controller. Let $\mathbf{p}_b = [x_b, y_b, z_b]^T \in \mathbb{R}^3, \forall b \in \mathcal{B}$ be the tuple denoting the location of the b -th radiating element, where each element is modelled as a point [43]. Using the primary element as the reference leads to

$$x_b = d_x \times \text{mod}(b-1, B_x), \forall b \in \mathcal{B}, \quad (1a)$$

$$z_b = d_z \times \lfloor (b-1)/B_x \rfloor, \forall b \in \mathcal{B}, \quad (1b)$$

with d_x and d_z being the element spacing in the UPA's x - and z -axis directions, respectively, which are usually set as $d_x = d_z = \lambda/2$.

Additionally, the y -coordinate of each radiating element satisfies the constraint [43]

$$y_{\min} \leq y_b \leq y_{\max}, \forall b \in \mathcal{B}, \quad (1c)$$

where y_{\min} and y_{\max} represent the minimum and maximum y -coordinate allowed for each radiating element, and we define $\zeta \triangleq y_{\min} - y_{\max} > 0$ to be the *morphing range* characterizing the FIM, where we henceforth set Without loss of generality (wlg), $y_{\min} = 0$, Wlg.

Subsequently, the distinguishing shape of a FIM is given by

$$\mathbf{y} \triangleq [y_1, y_2, \dots, y_B]^T \in \mathbb{R}_+^{B \times 1}. \quad (2)$$

Then, the response vector $\mathbf{b}(\mathbf{y}, \phi, \theta) \in \mathbb{C}^{B \times 1}$ corresponding to a path impinging onto (or outgoing from) the array is given as

$$\mathbf{b}(\mathbf{y}, \phi, \theta) \triangleq \frac{1}{\sqrt{B}} \left[1, e^{j\frac{2\pi}{\lambda} (x_1 \sin(\theta) \cos(\phi) + y_1 \sin(\theta) \sin(\phi) + z_1 \cos(\theta))}, \dots, e^{j\frac{2\pi}{\lambda} (x_B \sin(\theta) \cos(\phi) + y_B \sin(\theta) \sin(\phi) + z_B \cos(\theta))} \right]^T. \quad (3)$$

B. FIM MIMO Channel Model

Leveraging the above, the MIMO DD channel model with FIMs at both the transmitter and receiver $\mathbf{H}(\mathbf{y}_T, \mathbf{y}_R, t, \tau) \in \mathbb{C}^{N_R \times N_T}$ is given by

$$\mathbf{H}(\mathbf{y}_T, \mathbf{y}_R, t, \tau) \triangleq \sqrt{\frac{N_T N_R}{P}} \sum_{p=1}^P h_p e^{j2\pi\nu_p t} \delta(\tau - \tau_p) \times \mathbf{b}_{R:p}(\mathbf{y}_R, \phi_p^{\text{in}}, \theta_p^{\text{in}}) \mathbf{b}_{T:p}^H(\mathbf{y}_T, \phi_p^{\text{out}}, \theta_p^{\text{out}}), \quad (4)$$

where $\mathbf{b}_{T:p}(\cdot, \cdot, \cdot) \in \mathbb{C}^{N_T \times 1}$ and $\mathbf{b}_{R:p}(\cdot, \cdot, \cdot) \in \mathbb{C}^{N_R \times 1}$ are respectively the FIM UPA response vectors for the TX and RX defined in equation (3) containing N_T and N_R elements, with $(\mathbf{y}_R, \phi_p^{\text{in}}, \theta_p^{\text{in}})$ and $(\mathbf{y}_T, \phi_p^{\text{out}}, \theta_p^{\text{out}})$ containing the FIM shaping vector and pairs of azimuth and elevation AoAs and AoDs, respectively, for each p -th signal propagation path having the complex channel gain h_p , with $p = \{1, \dots, P\}$. In the above, $\tau_p \in [0, \tau_{\max}]$ and $\nu_p \in [-\nu_{\max}, \nu_{\max}]$ denote each p -th path's delay in seconds and Doppler shift in Hz, respectively³.

TABLE I: Variable Notation and Descriptions.

Variable	Description
N_T, N_R	Number of TX and RX FIM elements
$\theta_p^{\text{in}}, \theta_p^{\text{out}}$	AoA and AoD elevation angle
$\phi_p^{\text{in}}, \phi_p^{\text{out}}$	AoA and AoD azimuth angle
h_p	p -th complex channel gain
τ_p	p -th associated delay
ν_p	p -th associated Doppler shift
$\mathbf{b}_{T:p}(\cdot, \cdot, \cdot)$	p -th TX FIM UPA response vector
$\mathbf{b}_{R:p}(\cdot, \cdot, \cdot)$	p -th RX FIM UPA response vector
$\mathbf{H}(\mathbf{y}_T, \mathbf{y}_R, t, \tau)$	FIM MIMO channel model

³While the motion of the FIMs also causes slight variations in the relative τ_p and ν_p , this effect is negligible when the FIM movement is restricted to be a factor of λ as in [43].

$$\mathbf{r}[n] = \sum_{\ell=0}^{\infty} \left[\underbrace{\left(\sum_{p=1}^P \sqrt{\frac{N_T N_R}{P}} h_p \mathbf{U}^H \mathbf{b}_{R:p}(\mathbf{y}_R, \phi_p^{\text{in}}, \theta_p^{\text{in}}) \mathbf{b}_{T:p}^H(\mathbf{y}_T, \phi_p^{\text{out}}, \theta_p^{\text{out}}) \mathbf{V} e^{j2\pi f_p \frac{n}{N}} \delta[\ell - \ell_p] \right)}_{\check{\mathbf{H}}_p(\mathbf{y}_T, \mathbf{y}_R) \in \mathbb{C}^{d_s \times d_s}} \mathbf{s}[n - \ell] \right] + \mathbf{w}[n] \quad (6)$$

$$\mathbf{r}_v = \sum_{u=1}^{d_s} \sum_{p=1}^P \underbrace{\check{h}_{p,v,u}}_{\substack{\triangleq \check{\mathbf{H}}_{v,u}(\mathbf{y}_T, \mathbf{y}_R) \in \mathbb{C}^{N \times N} \\ \triangleq \mathbf{G}_p \in \mathbb{C}^{N \times N}}} \mathbf{s}_u + \mathbf{w}_v = \sum_{u=1}^{d_s} \check{\mathbf{H}}_{v,u}(\mathbf{y}_T, \mathbf{y}_R) \mathbf{s}_u + \mathbf{w}_v \quad (7)$$

$$\mathbf{\Theta}_p \triangleq \text{diag} \left(\underbrace{[e^{-j2\pi\phi_{\text{CP}}(\ell_p)}, e^{-j2\pi\phi_{\text{CP}}(\ell_p-1)}, \dots, e^{-j2\pi\phi_{\text{CP}}(2)}, e^{-j2\pi\phi_{\text{CP}}(1)}]}_{\ell_p \text{ terms}}, \underbrace{1, 1, \dots, 1}_{N - \ell_p \text{ ones}} \right) \in \mathbb{C}^{N \times N} \quad (8)$$

$$\mathbf{\Omega} \triangleq \text{diag}([1, e^{-j2\pi/N}, \dots, e^{-j2\pi(N-2)/N}, e^{-j2\pi(N-1)/N}]) \in \mathbb{C}^{N \times N} \quad (9)$$

III. I/O RELATIONSHIPS FOR OFDM, OTFS, AND AFDM

In this section, leveraging the previously proposed FPDD channel model, we present various expressions for the time-domain (TD) received signal corresponding to waveforms such as OFDM, OTFS, and AFDM. The framework presented is general and also incorporates hybrid analog and digital beamformers, which can be optimized for further performance improvements [45].

A. Arbitrarily Modulated Signals

The point-to-point MIMO configuration illustrated in Fig. 1 employs hybrid analog-digital beamformers at its N_T -element TX and N_R -element RX, following a similar structure to [46].

Let $\mathbf{V} \in \mathbb{C}^{N_T \times d_s}$ and $\mathbf{U} \in \mathbb{C}^{N_R \times d_s}$ denote the hybrid beamformers for transmission and reception, respectively, where $d_s \triangleq \min(N_T, N_R)$ represents the number of independent data streams transmitted per coherent channel block. In the following, the complex-valued vector $\mathbf{s}(t) \in \mathbb{C}^{d_s \times 1}$ is the power-constrained transmit signal, which can employ either OFDM, OTFS, or AFDM in the TD.

The d_s -element baseband signal received at time t (post-hybrid combining) through the FIM MIMO channel is mathematically expressed as

$$\begin{aligned} \mathbf{r}(t) &\triangleq \mathbf{U}^H \mathbf{H}(\mathbf{y}_T, \mathbf{y}_R, t, \tau) * \mathbf{V} \mathbf{s}(t) + \mathbf{w}(t) \\ &= \int_{-\infty}^{\infty} \mathbf{U}^H \mathbf{H}(\mathbf{y}_T, \mathbf{y}_R, t, \tau) \mathbf{V} \mathbf{s}(t - \tau) d\tau + \mathbf{w}(t), \end{aligned} \quad (5)$$

where $\mathbf{w}(t) \triangleq \mathbf{U}^H \mathbf{n}(t) \in \mathbb{C}^{d_s \times 1}$ and $\mathbf{n}(t) \in \mathbb{C}^{N_R \times 1}$ represents the additive white Gaussian noise (AWGN) vector at the RX, with elements that are uncorrelated both spatially and temporally, each having zero mean and variance σ_n^2 .

Let $\mathbf{r}[n] \in \mathbb{C}^{d_s \times 1}$ and $\mathbf{s}[n] \in \mathbb{C}^{d_s \times 1}$, with $n \in \{0, \dots, N-1\}$, be the discrete sequences derived by sampling $\mathbf{r}(t)$ and $\mathbf{s}(t)$, respectively, at a sufficiently high rate $F_s \triangleq \frac{1}{T_s}$ in Hz within a bandwidth B [47]. The discrete-time form of the received signal in equation (5) is presented (at the top of the page) in equation (6), where ℓ denotes the normalized discrete delay index, and $f_p \triangleq \frac{N\nu_p}{F_s}$ and $\ell_p \triangleq \frac{T_p}{T_s}$ represent the normalized Doppler shift and the corresponding normalized

discrete delay index for each p -th propagation path between the TX-FIM and RX-FIM, respectively.

Considering a cyclic prefix (CP) of length N_{CP} and employing circular convolution, the N -element discrete-time received signal in equation (6) can be reformulated [13] as shown in equation (7), where, for simplicity, the discrete-time index is omitted (and will be henceforth). In this equation, the scalars $\check{h}_{p,v,u}$ with $(v, u) = \{1, \dots, d_s\}$ are the (v, u) -th elements of the matrix $\check{\mathbf{H}}_p(\mathbf{y}_T, \mathbf{y}_R)$, implicitly defined in equation (6). Furthermore, $\mathbf{s}_u \triangleq [s_u[0], \dots, s_u[N-1]] \in \mathbb{C}^{N \times 1}$ and $\mathbf{w}_v \triangleq [w_v[0], \dots, w_v[N-1]] \in \mathbb{C}^{N \times 1}$ represent the transmit signal and AWGN vectors for the u -th and v -th streams, respectively.

Each diagonal matrix $\mathbf{\Theta}_p \in \mathbb{C}^{N \times N}$, defined in equation (8), accounts for the effect of the CP on the p -th channel path, with $\phi_{\text{CP}}(n)$ being a phase function dependent on the sample index $n \in \{0, \dots, N-1\}$, varying with the specific waveform employed. Additionally, the diagonal matrix $\mathbf{\Omega} \in \mathbb{C}^{N \times N}$, defined in equation (9), comprises N complex roots of unity, while $\mathbf{\Pi} \in \{0, 1\}^{N \times N}$ is the forward cyclic shift matrix with elements defined as

$$\pi_{i,j} \triangleq \delta_{i,j+1} + \delta_{i,j-(N-1)} \quad \delta_{ij} \triangleq \begin{cases} 0 & \text{if } i \neq j \\ 1 & \text{if } i = j \end{cases}. \quad (10)$$

Using the Kronecker product to combine all d_s \mathbf{r}_v vectors in equation (7), the resulting Nd_s -element vector for the overall received signal in the TD, for an arbitrarily modulated transmit signal, is expressed as

$$\mathbf{r}_{\text{TD}} = \bar{\mathbf{H}}(\mathbf{y}_T, \mathbf{y}_R) \mathbf{s}_{\text{TD}} + \bar{\mathbf{w}}_{\text{TD}}, \quad (11)$$

where $\bar{\mathbf{H}}(\mathbf{y}_T, \mathbf{y}_R) \in \mathbb{C}^{Nd_s \times Nd_s}$ explicitly reflects the dependence of the TD transfer function of the point-to-point MIMO system on the TX and RX FIMs, and is defined as

$$\bar{\mathbf{H}}(\mathbf{y}_T, \mathbf{y}_R) \triangleq \sum_{p=1}^P (\check{\mathbf{H}}_p(\mathbf{y}_T, \mathbf{y}_R) \otimes \mathbf{G}_p), \quad (12)$$

with the Nd_s -element vectors \mathbf{s}_{TD} and $\bar{\mathbf{w}}_{\text{TD}}$ formed by concatenating \mathbf{s}_u and \mathbf{w}_v from equation (7), respectively.

For notational brevity, the matrix $\check{\mathbf{H}}_p$ in equation (12) will henceforth be written without explicitly noting its dependence on the TX/RX FIM parameters.

B. OFDM Signaling

Let \mathcal{C} represent an arbitrary complex constellation set with cardinality D and average energy E_S , associated with a specific digital modulation scheme (e.g., quadrature amplitude modulation (QAM)). In OFDM, multiple information vectors $\mathbf{x}_u \in \mathbb{C}^{N \times 1}$, where $u = \{1, \dots, d_s\}$, comprising a total of Nd_s symbols, are modulated into the transmit signal as

$$\mathbf{s}_u^{(\text{OFDM})} \triangleq \mathbf{F}_N^H \mathbf{x}_u \in \mathbb{C}^{N \times 1}, \quad (13)$$

where \mathbf{F}_N is the N -point normalized DFT matrix.

After circular convolution with the DD channel and following a formulation akin to equation (11), the corresponding Nd_s -element discrete-time received OFDM signal is expressed as

$$\mathbf{r}_{\text{OFDM}} \triangleq \bar{\mathbf{H}}(\mathbf{y}_T, \mathbf{y}_R) \mathbf{s}_{\text{OFDM}} + \bar{\mathbf{w}}_{\text{TD}}, \quad (14)$$

where the Nd_s -element vectors are defined as

$$\mathbf{s}_{\text{OFDM}} \triangleq \begin{bmatrix} \mathbf{s}_1^{(\text{OFDM})} \\ \vdots \\ \mathbf{s}_{d_s}^{(\text{OFDM})} \end{bmatrix}, \quad \mathbf{r}_{\text{OFDM}} \triangleq \begin{bmatrix} \mathbf{r}_1^{(\text{OFDM})} \\ \vdots \\ \mathbf{r}_{d_s}^{(\text{OFDM})} \end{bmatrix}. \quad (15)$$

At the RX, applying OFDM demodulation results in

$$\mathbf{y}_v^{(\text{OFDM})} \triangleq \mathbf{F}_N \mathbf{r}_v^{(\text{OFDM})} \in \mathbb{C}^{N \times 1}, \quad (16)$$

yielding the corresponding Nd_s -element discrete-time signal

$$\mathbf{y}_{\text{OFDM}} = \bar{\mathbf{H}}_{\text{OFDM}}(\mathbf{y}_T, \mathbf{y}_R) \mathbf{x} + \bar{\mathbf{w}}_{\text{OFDM}}, \quad (17)$$

where $\bar{\mathbf{w}}_{\text{OFDM}} \in \mathbb{C}^{Nd_s \times 1}$ is an equivalent AWGN with the same statistics as $\bar{\mathbf{w}}_{\text{TD}}$, and $\bar{\mathbf{H}}_{\text{OFDM}}(\mathbf{y}_T, \mathbf{y}_R) \in \mathbb{C}^{Nd_s \times Nd_s}$ denotes the effective OFDM channel, defined similarly to $\bar{\mathbf{H}}(\mathbf{y}_T, \mathbf{y}_R)$ in equation (11) as

$$\begin{aligned} \bar{\mathbf{H}}_{\text{OFDM}}(\mathbf{y}_T, \mathbf{y}_R) &\triangleq \sum_{p=1}^P \check{\mathbf{H}}_p \otimes \overbrace{(\mathbf{F}_N \mathbf{G}_p \mathbf{F}_N^H)}^{\triangleq \mathbf{G}_p^{\text{OFDM}} \in \mathbb{C}^{N \times N}} \\ &= \sum_{p=1}^P \check{\mathbf{H}}_p \otimes \mathbf{G}_p^{\text{OFDM}}. \end{aligned} \quad (18)$$

Note that for OFDM, the CP phase matrices Θ_p 's in equation (7) simplify to identity matrices [13], i.e., $\phi_{\text{CP}}(n) = 0$ in equation (8), as there is no phase offset.

C. OTFS Signaling

When employing OTFS, multiple matrices $\mathbf{X}_u \in \mathbb{C}^{\tilde{K} \times \tilde{K}'}$, with $u = \{1, \dots, d_s\}$, containing $\tilde{K}\tilde{K}'d_s$ symbols from an arbitrary complex constellation \mathcal{C} , are modulated as⁴

$$\mathbf{s}_u^{(\text{OTFS})} \triangleq \text{vec}(\mathbf{S}_u) = (\mathbf{F}_{\tilde{K}}^H \otimes \mathbf{I}_{\tilde{K}'}) \text{vec}(\mathbf{X}_u) \in \mathbb{C}^{\tilde{K}\tilde{K}' \times 1}, \quad (19)$$

where $\text{vec}(\cdot)$ denotes matrix vectorization via column stacking and \mathbf{S}_u is a TD symbols' matrix obtained from⁵ the inverse discrete Zak transform (IDZT) of \mathbf{X}_u as [14]

$$\mathbf{S}_u = \mathbf{X}_u \mathbf{F}_{\tilde{K}}^H \in \mathbb{C}^{\tilde{K} \times \tilde{K}'}. \quad (20)$$

⁴For simplicity, we assume that all pulse-shaping operations utilize rectangular waveforms such that the corresponding sample matrices can be reduced to identity matrices.

⁵Equivalently, \mathbf{S}_u can be obtained as the Heisenberg transform of the inverse symplectic finite Fourier transform (ISFFT) of \mathbf{X}_u , i.e., $\mathbf{S}_u = \mathbf{F}_{\tilde{K}}^H \mathbf{X}_{\text{FT}}^u$ with $\mathbf{X}_{\text{FT}}^u \triangleq \mathbf{F}_{\tilde{K}} \mathbf{X}_u \mathbf{F}_{\tilde{K}'}^H \in \mathbb{C}^{\tilde{K} \times \tilde{K}'}$.

It is noted that the notation in equation (19) aligns with the approach in [48], where OTFS signals are vectorized and augmented with a CP of length N_{CP} to mitigate inter-frame interference, similar to OFDM. To facilitate direct comparisons between these waveforms, we set $\tilde{K} \times \tilde{K}' = N$ henceforth.

Following transmission over the DD channel $\bar{\mathbf{H}}(\mathbf{y}_T, \mathbf{y}_R)$ as in equation (11), the Nd_s -element discrete-time received OTFS signal is modeled similarly to equation (14) as $\mathbf{r}_{\text{OTFS}} \triangleq \bar{\mathbf{H}}(\mathbf{y}_T, \mathbf{y}_R) \mathbf{s}_{\text{OTFS}} + \bar{\mathbf{w}}_{\text{TD}}$, where \mathbf{s}_{OTFS} and \mathbf{r}_{OTFS} are defined for OTFS analogously to equation (15).

Unlike OFDM, detecting the information symbols \mathbf{X}_u from the $\mathbf{r}_v^{(\text{OTFS})}$ elements ($\forall v = 1, \dots, d_s$) of \mathbf{r}_{OTFS} requires undoing the vectorization and IDZT operations used to construct the d_s elements of \mathbf{s}_{OTFS} , leading to a unique effective channel. Specifically, let $\mathbf{R}_v \triangleq \text{vec}^{-1}(\mathbf{r}_v^{(\text{OTFS})}) \in \mathbb{C}^{\tilde{K} \times \tilde{K}'}$, with $\text{vec}^{-1}(\cdot)$ indicating the de-vectorization operation according to which a vector of size $\tilde{K}\tilde{K}' \times 1$ is reshaped into a matrix of size $\tilde{K} \times \tilde{K}'$, and consider the following discrete Zak transform (DZT)⁶

$$\mathbf{Y}_v = \mathbf{R}_v \mathbf{F}_{\tilde{K}'} \in \mathbb{C}^{\tilde{K} \times \tilde{K}'}. \quad (21)$$

The demodulated OTFS signal at the RX is then given by

$$\mathbf{y}_v^{(\text{OTFS})} \triangleq \text{vec}(\mathbf{Y}_v) = (\mathbf{F}_{\tilde{K}'} \otimes \mathbf{I}_{\tilde{K}}) \mathbf{r}_v^{(\text{OTFS})} \in \mathbb{C}^{N \times 1}, \quad (22)$$

which can be compactly expressed, similar to equation (17), as the following Nd_s -element discrete-time received signal

$$\mathbf{y}_{\text{OTFS}} = \bar{\mathbf{H}}_{\text{OTFS}}(\mathbf{y}_T, \mathbf{y}_R) \mathbf{x} + \bar{\mathbf{w}}_{\text{OTFS}}, \quad (23)$$

where $\bar{\mathbf{w}}_{\text{OTFS}} \in \mathbb{C}^{Nd_s \times 1}$ is an equivalent AWGN with the same statistics as $\bar{\mathbf{w}}_{\text{TD}}$, and $\bar{\mathbf{H}}_{\text{OTFS}}(\mathbf{y}_T, \mathbf{y}_R) \in \mathbb{C}^{Nd_s \times Nd_s}$ represents the effective OTFS channel, given by

$$\begin{aligned} \bar{\mathbf{H}}_{\text{OTFS}}(\mathbf{y}_T, \mathbf{y}_R) &\triangleq \sum_{p=1}^P \check{\mathbf{H}}_p \otimes \overbrace{((\mathbf{F}_{\tilde{K}'} \otimes \mathbf{I}_{\tilde{K}}) \mathbf{G}_p (\mathbf{F}_{\tilde{K}}^H \otimes \mathbf{I}_{\tilde{K}}))}^{\triangleq \mathbf{G}_p^{\text{OTFS}} \in \mathbb{C}^{N \times N}} \\ &= \sum_{p=1}^P \check{\mathbf{H}}_p \otimes \mathbf{G}_p^{\text{OTFS}}. \end{aligned} \quad (24)$$

Similar to OFDM, the CP phase matrices Θ_p 's reduce to identity matrices [13]. By comparing equations (18) and (24), the channel modeling approach in [13] highlights both the structural similarities and the distinct effects of OFDM and OTFS waveforms in DD channels.

D. AFDM Signaling

The transmit signal for each information vector \mathbf{x}_u using the AFDM waveform in the considered FIM MIMO channel is obtained via the inverse discrete affine Fourier transform (IDAFST) as

$$\mathbf{s}_u^{(\text{AFDM})} \triangleq \mathbf{\Lambda}_1^H \mathbf{F}_N^H \mathbf{\Lambda}_2^H \mathbf{x}_u \in \mathbb{C}^{N \times 1}, \quad (25)$$

where the $N \times N$ matrices $\mathbf{\Lambda}_i$ with $i = 1, 2$ are defined as

$$\mathbf{\Lambda}_i \triangleq \text{diag}([1, e^{-j2\pi c_i 2^2}, \dots, e^{-j2\pi c_i (N-1)^2}]), \quad (26)$$

⁶Equivalently, \mathbf{Y}_v can be obtained as the SFFT of the Wigner transform of \mathbf{R}_v : $\mathbf{Y}_{\text{FT}}^v \triangleq \mathbf{F}_{\tilde{K}} \mathbf{R}_v$, yielding $\mathbf{Y}_v = \mathbf{F}_{\tilde{K}}^H \mathbf{Y}_{\text{FT}}^v \mathbf{F}_{\tilde{K}'} \in \mathbb{C}^{\tilde{K} \times \tilde{K}'}$.

$$\Theta_p \triangleq \text{diag} \left(\underbrace{[e^{-j2\pi c_1(N^2-2N\ell_p)}, e^{-j2\pi c_1(N^2-2N(\ell_p-1))}, \dots, e^{-j2\pi c_1(N^2-2N)}]_{\ell_p \text{ terms}}}_{\ell_p \text{ terms}}, \underbrace{[1, 1, \dots, 1]_{N-\ell_p \text{ ones}}}_{N-\ell_p \text{ ones}} \right) \in \mathbb{C}^{N \times N} \quad (27)$$

where the first central chirp frequency c_1 is an optimized parameter based on maximum Doppler channel statistics [13], [49], and the second central chirp frequency c_2 is a flexible parameter that can be used for ISAC waveform shaping [50] or information encoding [51], [52].

As shown in [13], after transmission through a DD channel, an AFDM modulated symbol vector $\mathbf{s}_u^{(\text{AFDM})}$ with a *chirp-periodic* prefix (CPP) can be modeled similarly to equation (7) by replacing the CP matrix Θ_p in equation (8) with the CPP matrix Θ_p given by equation (27) (top of this page). This requires setting the function $\phi_{\text{CP}}(n)$ in equation (8) as $\phi_{\text{CP}}(n) = c_1(N^2 - 2Nn)$. Thus, the Nd_s -element discrete-time received AFDM signal can be modeled similarly to equation (14) as $\mathbf{r}_{\text{AFDM}} \triangleq \bar{\mathbf{H}}(\mathbf{y}_T, \mathbf{y}_R) \mathbf{s}_{\text{AFDM}} + \bar{\mathbf{w}}_{\text{TD}}$, where \mathbf{s}_{AFDM} and \mathbf{r}_{AFDM} are defined for AFDM analogously to equation (15).

The AFDM demodulation of each of the $\mathbf{r}_v^{(\text{AFDM})}$ with $v \in \{1, \dots, d_s\}$ elements of \mathbf{r}_{AFDM} is obtained as

$$\mathbf{y}_v^{(\text{AFDM})} = \mathbf{\Lambda}_2 \mathbf{F}_N \mathbf{\Lambda}_1 \mathbf{r}_v^{(\text{AFDM})} \in \mathbb{C}^{N \times 1}, \quad (28)$$

yielding the following expression for the Nd_s -element discrete-time received signal (similar to equations (17) and (23))

$$\mathbf{y}_{\text{AFDM}} = \bar{\mathbf{H}}_{\text{AFDM}}(\mathbf{y}_T, \mathbf{y}_R) \mathbf{x} + \bar{\mathbf{w}}_{\text{AFDM}}, \quad (29)$$

where $\bar{\mathbf{w}}_{\text{AFDM}} \in \mathbb{C}^{Nd_s \times 1}$ is an equivalent AWGN with the same statistics as $\bar{\mathbf{w}}_{\text{TD}}$, and $\bar{\mathbf{H}}_{\text{AFDM}}(\mathbf{y}_T, \mathbf{y}_R) \in \mathbb{C}^{Nd_s \times Nd_s}$ represents the effective AFDM channel, given by

$$\begin{aligned} \bar{\mathbf{H}}_{\text{AFDM}}(\mathbf{y}_T, \mathbf{y}_R) &\triangleq \sum_{p=1}^P \check{\mathbf{H}}_p \otimes \underbrace{(\mathbf{\Lambda}_2 \mathbf{F}_N \mathbf{\Lambda}_1 \mathbf{G}_p \mathbf{\Lambda}_1^H \mathbf{F}_N^H \mathbf{\Lambda}_2^H)}_{\mathbf{G}_p^{\text{AFDM}} \in \mathbb{C}^{N \times N}} \quad (30) \\ &= \sum_{p=1}^P \check{\mathbf{H}}_p \otimes \mathbf{G}_p^{\text{AFDM}}. \end{aligned}$$

Evidently, equation (30) shares the same structure as equations (18) and (24), as do the MIMO input-output relationships in equations (17), (23), and (29). This suggests that signal processing techniques, such as channel estimation, can be developed within a unified framework applicable to OFDM, OTFS, AFDM, and similar waveforms.

IV. FIM OPTIMIZATION FOR ISAC

In this paper, we aim to maximize both the communication and sensing performances by tuning both the TX-FIM and RX-FIM under the information-theoretical achievable rate criteria and a practical sensing constraint that makes sure the signal power at a certain scatterer achieves a certain threshold, as described below.

A. Problem Formulation

Under an information-theoretical approach, the FIM optimization problem seeks to maximize the achievable rate of the

MIMO channel between a pair of FIMs by jointly optimizing the 3D surface shapes \mathbf{y}_T and \mathbf{y}_R of the transmitting and receiving FIMs, and the transmit covariance matrix $\mathbf{T} \triangleq \mathbf{x}\mathbf{x}^H$, subject to the morphing range of these two FIMs, a total transmit power constraint P_t , and the sensing QoS which aims to make sure that the signal power at the target locations achieve a certain threshold Ψ . Specifically, the joint optimization problem can be formulated as

$$\max_{\mathbf{T}, \mathbf{y}_T, \mathbf{y}_R} \log_2 \det \left(\mathbf{I}_{Nd_s} + \frac{1}{\sigma_w^2} \bar{\mathbf{H}}(\mathbf{y}_T, \mathbf{y}_R) \mathbf{T} \bar{\mathbf{H}}^H(\mathbf{y}_T, \mathbf{y}_R) \right) \quad (31a)$$

$$\text{s.t.} \quad \text{tr}(\mathbf{T}) \leq P_t, \quad \mathbf{T} \succeq \mathbf{0}, \quad (31b)$$

$$\text{tr}(\bar{\mathbf{H}}(\mathbf{y}_T, \mathbf{y}_R) \mathbf{T} \bar{\mathbf{H}}^H(\mathbf{y}_T, \mathbf{y}_R)) \geq \Psi, \quad (31c)$$

$$\mathbf{y}_T = [y_{T,1}, y_{T,2}, \dots, y_{T,N_T}]^T, \quad (31d)$$

$$\mathbf{y}_R = [y_{R,1}, y_{R,2}, \dots, y_{R,N_R}]^T, \quad (31e)$$

$$y_{\min} \leq y_{T,n_T} \leq y_{\max}, \quad n_T = 1, 2, \dots, N_T, \quad (31f)$$

$$y_{\min} \leq y_{R,n_R} \leq y_{\max}, \quad n_R = 1, 2, \dots, N_R, \quad (31g)$$

where (31b) characterizes the transmit power constraint, while (31d) – (31g) characterize the constraints on adjusting the deformation range for each antenna on the transmitting and receiving FIMs.

In addition, $\bar{\mathbf{H}}(\mathbf{y}_T, \mathbf{y}_R)$ represents the general effective channel regardless of the waveform used. Furthermore, for clarity of exposition, let us restate that the matrices to be optimized $\bar{\mathbf{H}}_p(\mathbf{y}_T, \mathbf{y}_R) \in \mathbb{C}^{N_R \times N_T}$ are encapsulated inside

$$\bar{\mathbf{H}}(\mathbf{y}_T, \mathbf{y}_R) = \sum_{p=1}^P \left(\check{\mathbf{H}}_p(\mathbf{y}_T, \mathbf{y}_R) \otimes \bar{\mathbf{G}}_p \right), \quad (32)$$

where $\check{\mathbf{H}}_p(\mathbf{y}_T, \mathbf{y}_R)$ – without considering digital beamforming – can be expressed as

$$\check{\mathbf{H}}_p(\mathbf{y}_T, \mathbf{y}_R) = \tilde{h}_p \mathbf{b}_{R:p}(\mathbf{y}_R, \phi_p^{\text{in}}, \theta_p^{\text{in}}) \mathbf{b}_{T:p}^H(\mathbf{y}_T, \phi_p^{\text{out}}, \theta_p^{\text{out}}), \quad (33)$$

with $\bar{\mathbf{G}}_p$ representing an arbitrary channel matrix resulting from any aforementioned waveform and $\tilde{h}_p \triangleq \sqrt{\frac{N_T N_R}{P}} h_p$.

To efficiently solve this non-convex problem, we can first reformulate it leveraging a mixed objective for the regularization term by defining $g_c = \min\{\text{tr}(\bar{\mathbf{H}}(\mathbf{y}_T, \mathbf{y}_R) \mathbf{T} \bar{\mathbf{H}}^H(\mathbf{y}_T, \mathbf{y}_R)) - \Psi, 0\}$ as

$$\max_{\mathbf{T}, \mathbf{y}_T, \mathbf{y}_R} \log_2 \det \left(\mathbf{I}_{Nd_s} + \frac{1}{\sigma_w^2} \bar{\mathbf{H}}(\mathbf{y}_T, \mathbf{y}_R) \mathbf{T} \bar{\mathbf{H}}^H(\mathbf{y}_T, \mathbf{y}_R) \right) + \beta g_c \quad (34a)$$

$$\text{s.t.} \quad \text{tr}(\mathbf{T}) \leq P_t, \quad \mathbf{T} \succeq \mathbf{0}, \quad (34b)$$

$$\mathbf{y}_T = [y_{T,1}, y_{T,2}, \dots, y_{T,N_T}]^T, \quad (34c)$$

$$\mathbf{y}_R = [y_{R,1}, y_{R,2}, \dots, y_{R,N_R}]^T, \quad (34d)$$

$$y_{\min} \leq y_{T,n_T} \leq y_{\max}, \quad n_T = 1, 2, \dots, N_T, \quad (34e)$$

$$y_{\min} \leq y_{R,n_R} \leq y_{\max}, \quad n_R = 1, 2, \dots, N_R, \quad (34f)$$

where $\beta \in \mathbb{R}^+$ is a penalty factor denoting the tradeoff between the achievable rate and sensing QoS.

Before solving the aforementioned optimization problem, let us clarify that the optimization of the transmit covariance matrix \mathbf{T} in equation (34) in the considered system⁷ would require some non-trivial techniques such as adaptive modulation. Since we already consider \mathbf{x} to be picked from a discrete constellation such that the individual symbols are random and independent and identically distributed (i.i.d.), in the limit when the product Nd_s grows large, $\mathbf{T} \rightarrow \mathbf{I}_{Nd_s}$. Therefore, for the sake of simplicity and to explicitly highlight the effects of the FIM, we hereafter consider that $\mathbf{T} \approx \mathbf{I}_{Nd_s}$. We can now obtain a suboptimal solution to the problem in equation (31) by solving the reformulated problem in equation (34).

B. Proposed Optimization Framework

Leveraging the assumption on \mathbf{T} , the optimization problem in equation (34) can be solved for the FIM parameters \mathbf{y}_T and \mathbf{y}_R as follows. First, substituting $\mathbf{T} = \mathbf{I}_{Nd_s}$ yields

$$\max_{\mathbf{y}_T, \mathbf{y}_R} \log_2 \det \left(\mathbf{I}_{Nd_s} + \frac{1}{\sigma_w^2} \overbrace{\bar{\mathbf{H}}(\mathbf{y}_T, \mathbf{y}_R) \bar{\mathbf{H}}^H(\mathbf{y}_T, \mathbf{y}_R)}^{\mathbf{Q}} \right) + \beta g_c \quad (35a)$$

$$\text{s.t.} \quad \mathbf{y}_T = [y_{T,1}, y_{T,2}, \dots, y_{T,N_T}]^T, \quad (35b)$$

$$\mathbf{y}_R = [y_{R,1}, y_{R,2}, \dots, y_{R,N_R}]^T, \quad (35c)$$

$$y_{\min} \leq y_{T,n_T} \leq y_{\max}, \quad n_T = 1, 2, \dots, N_T, \quad (35d)$$

$$y_{\min} \leq y_{R,n_R} \leq y_{\max}, \quad n_R = 1, 2, \dots, N_R. \quad (35e)$$

However, since an optimal closed-form solution to equation (35) is still difficult to obtain, we can leverage the gradient ascent algorithm to search for a sub-optimal solution. Specifically, given the surface shapes of the transmitting and receiving FIMs obtained from a previous iteration, we can adjust their surface shape configurations towards the direction of the gradient for gradually increasing the achievable rate subject to the QoS sensing constraint as well. The gradient ascent algorithm involves two major steps: 1) a gradient calculation, and 2) a surface shape update.

1) Gradient Calculation: In order to develop an efficient gradient-ascent algorithm, we need to first calculate the closed-form gradients of the expression $\frac{\partial \bar{\mathbf{H}}(\mathbf{y}_T, \mathbf{y}_R)}{\partial \mathbf{y}_T}$ in a tractable manner. However, since $\bar{\mathbf{H}}(\mathbf{y}_T, \mathbf{y}_R)$ is a matrix and \mathbf{y}_T is a vector, the gradient $\frac{\partial \bar{\mathbf{H}}(\mathbf{y}_T, \mathbf{y}_R)}{\partial \mathbf{y}_T}$ becomes a tensor of size $Nd_s \times Nd_s \times N_T$ leading to cumbersome expressions later on. Therefore, for ease of implementation as well as tractability, we focus on gradients per element of \mathbf{y}_T , hereafter denoted by $\mathbf{y}_{T:n_t}$, with the equivalent partial derivative denoted by $\frac{\partial \bar{\mathbf{H}}(\mathbf{y}_T, \mathbf{y}_R)}{\partial \mathbf{y}_{T:n_t}} \in \mathbb{C}^{Nd_s \times Nd_s}$.

Let us start with the fact that $\mathbf{y}_{T:n_t}$ only depends on $\mathbf{b}_{T:p}^H(\mathbf{y}_T, \phi_p^{\text{out}}, \theta_p^{\text{out}})$ to express the partial derivative of $\bar{\mathbf{H}}(\mathbf{y}_T, \mathbf{y}_R)$ with respect to $\mathbf{y}_{T:n_t}$ using equation (32) as

$$\frac{\partial \bar{\mathbf{H}}(\mathbf{y}_T, \mathbf{y}_R)}{\partial \mathbf{y}_{T:n_t}} = \sum_{p=1}^P \left(\left(\tilde{h}_p \mathbf{b}_{R:p}(\mathbf{y}_R) \frac{\partial \mathbf{b}_{T:p}^H(\mathbf{y}_T)}{\partial \mathbf{y}_{T:n_t}} \right) \otimes \bar{\mathbf{G}}_p \right), \quad (36)$$

⁷In principle, one can define a precoder $\tilde{\mathbf{U}}$ such that $\tilde{\mathbf{x}} \triangleq \tilde{\mathbf{U}}\mathbf{x}$ and $\mathbf{T} \triangleq \tilde{\mathbf{x}}\tilde{\mathbf{x}}^H = \tilde{\mathbf{U}}\mathbf{x}\mathbf{x}^H\tilde{\mathbf{U}}^H$ correspondingly to optimize $\tilde{\mathbf{U}}$, but this problem is relegated to future work.

where we drop the implicit dependence on the AoAs and AoDs for brevity, with $\frac{\partial \mathbf{b}_{T:p}^H(\mathbf{y}_T)}{\partial \mathbf{y}_{T:n_t}} \in \mathbb{C}^{1 \times N_T}$ defined as

$$\frac{\partial \mathbf{b}_{T:p}^H(\mathbf{y}_T)}{\partial \mathbf{y}_{T:n_t}} \triangleq \left(j \frac{2\pi}{\lambda} \sin(\phi_p^{\text{out}}) \sin(\theta_p^{\text{out}}) (\mathbf{e}_{n_t} \odot \mathbf{b}_{T:p}(\mathbf{y}_T)) \right)^H, \quad (37)$$

where $\mathbf{e}_{n_t} \in \mathbb{C}^{N_T \times 1}$ denotes a standard basis vector with 1 at the n_t -th position and zeros elsewhere while \odot denotes the Hardamard product.

Next, the full gradient of \mathbf{Q} with respect to $\mathbf{y}_{T:n_t}$ – which is a matrix of size $Nd_s \times Nd_s$ – can then be expressed as

$$\frac{\partial \mathbf{Q}}{\partial \mathbf{y}_{T:n_t}} = \frac{1}{\sigma_w^2} \left(\left(\frac{\partial \bar{\mathbf{H}}}{\partial \mathbf{y}_{T:n_t}} \right) \bar{\mathbf{H}}^H + \bar{\mathbf{H}} \left(\frac{\partial \bar{\mathbf{H}}}{\partial \mathbf{y}_{T:n_t}} \right)^H \right), \quad (38)$$

where we drop the inherent dependency on the variable for brevity.

Finally, denoting the objective function in equation (35a) by $f \triangleq \log_2 \det(\mathbf{I}_N + \mathbf{Q}) + \beta g_c$, the resulting scalar partial derivative per n_t -th element can be expressed as

$$\frac{\partial f}{\partial \mathbf{y}_{T:n_t}} = \frac{1}{\ln 2} \Re \left\{ \text{tr} \left((\mathbf{I}_{Nd_s} + \mathbf{Q})^{-1} \frac{\partial \mathbf{Q}}{\partial \mathbf{y}_{T:n_t}} \right) \right\} + \beta \frac{\partial g_c}{\partial \mathbf{y}_{T:n_t}}, \quad (39)$$

where

$$\frac{\partial g_c}{\partial \mathbf{y}_{T:n_t}} = \Re \left\{ \text{tr} \left(\left(\frac{\partial \bar{\mathbf{H}}}{\partial \mathbf{y}_{T:n_t}} \right) \bar{\mathbf{H}}^H + \bar{\mathbf{H}} \left(\frac{\partial \bar{\mathbf{H}}}{\partial \mathbf{y}_{T:n_t}} \right)^H \right) \right\}. \quad (40)$$

Algorithm 1 FIM Optimization for ISAC

Input: Gradient descent iterations i_{GD} and noise variance σ_w^2 .
Output: \mathbf{y}_T^* and \mathbf{y}_R^* .

Initialization

- Set iteration counter to $i = 0$.
 - Choose random $\mathbf{y}_T^* = \mathbf{y}_R^* = \mathbf{y}_{\text{init}}$ within morphing range.
 - Generate initial⁸ $\bar{\mathbf{H}}^*(\mathbf{y}_T^*, \mathbf{y}_R^*)$ from equation (32).
-

Surface Shape Optimization

for $i = 1$ to i_{GD} **do**:

- 1: Compute \mathbf{Q} from equation (35).
- for** $n_t = 1$ to N_T **do**:
- 2: Compute $\frac{\partial \mathbf{b}_{T:p}^H(\mathbf{y}_T)}{\partial \mathbf{y}_{T:n_t}}, \forall p$ from equation (37).
- 3: Compute $\frac{\partial \bar{\mathbf{H}}(\mathbf{y}_T, \mathbf{y}_R)}{\partial \mathbf{y}_{T:n_t}}$ from equation (36).
- 4: Compute $\frac{\partial \mathbf{Q}}{\partial \mathbf{y}_{T:n_t}}$ from equation (38).
- 5: Compute $\frac{\partial g_c}{\partial \mathbf{y}_{T:n_t}}$ from equation (40).
- 6: Compute $\frac{\partial f}{\partial \mathbf{y}_{T:n_t}}$ from equation (39).

end for

for $n_r = 1$ to N_R **do**:

- 7: Compute $\frac{\partial \mathbf{b}_{R:p}(\mathbf{y}_R)}{\partial \mathbf{y}_{R:n_r}}, \forall p$ from equation (42).
- 8: Compute $\frac{\partial \bar{\mathbf{H}}(\mathbf{y}_T, \mathbf{y}_R)}{\partial \mathbf{y}_{R:n_r}}$ from equation (41).
- 9: Compute $\frac{\partial \mathbf{Q}}{\partial \mathbf{y}_{R:n_r}}$ from equation (43).
- 10: Compute $\frac{\partial g_c}{\partial \mathbf{y}_{R:n_r}}$ from equation (45).
- 11: Compute $\frac{\partial f}{\partial \mathbf{y}_{R:n_r}}$ from equation (44).

end for

- 12: Update the surface shapes via equation (46).

end for

A similar procedure can now be used to calculate the partial derivative of $\bar{\mathbf{H}}(\mathbf{y}_T, \mathbf{y}_R)$ with respect to $\mathbf{y}_{R:n_r}$ using equation (32) as

$$\frac{\partial \bar{\mathbf{H}}(\mathbf{y}_T, \mathbf{y}_R)}{\partial \mathbf{y}_{R:n_r}} = \sum_{p=1}^P \left(\left(\tilde{h}_p \frac{\partial \mathbf{b}_{R:p}(\mathbf{y}_R)}{\partial \mathbf{y}_{R:n_r}} \mathbf{b}_{T:p}^H(\mathbf{y}_T) \right) \otimes \bar{\mathbf{G}}_p \right), \quad (41)$$

where we once again drop the implicit dependence on the AoAs and AoDs for brevity, with

$$\frac{\partial \mathbf{b}_{R:p}(\mathbf{y}_R)}{\partial \mathbf{y}_{R:n_r}} \triangleq j \frac{2\pi}{\lambda} \sin(\phi_p^{\text{in}}) \sin(\theta_p^{\text{in}}) (\mathbf{e}_{n_t} \odot \mathbf{b}_{R:p}(\mathbf{y}_R)). \quad (42)$$

Subsequently, the gradient of \mathbf{Q} with respect to $\mathbf{y}_{R:n_r}$ can then be expressed as

$$\frac{\partial \mathbf{Q}}{\partial \mathbf{y}_{R:n_r}} = \frac{1}{\sigma_w^2} \left(\left(\frac{\partial \bar{\mathbf{H}}}{\partial \mathbf{y}_{R:n_r}} \right) \bar{\mathbf{H}}^H + \bar{\mathbf{H}} \left(\frac{\partial \bar{\mathbf{H}}}{\partial \mathbf{y}_{R:n_r}} \right)^H \right), \quad (43)$$

where we drop the inherent dependency on the variable for brevity.

Correspondingly, the full partial derivative of the objective function with respect to $\mathbf{y}_{R:n_r}$ can be expressed as

$$\frac{\partial f}{\partial \mathbf{y}_{R:n_r}} = \frac{1}{\ln 2} \Re \left\{ \text{tr} \left((\mathbf{I}_{Nd_s} + \mathbf{Q})^{-1} \frac{\partial \mathbf{Q}}{\partial \mathbf{y}_{R:n_r}} \right) \right\} + \beta \frac{\partial g_c}{\partial \mathbf{y}_{R:n_r}}, \quad (44)$$

where

$$\frac{\partial g_c}{\partial \mathbf{y}_{R:n_r}} = \Re \left\{ \text{tr} \left(\left(\frac{\partial \bar{\mathbf{H}}}{\partial \mathbf{y}_{R:n_r}} \right) \bar{\mathbf{H}}^H + \bar{\mathbf{H}} \left(\frac{\partial \bar{\mathbf{H}}}{\partial \mathbf{y}_{R:n_r}} \right)^H \right) \right\}. \quad (45)$$

2) *Surface Shape Update*: Leveraging the gradients calculated above in equations (39) and (44), the parameter set contained in \mathbf{y}_T and \mathbf{y}_R at each i -th iteration can be updated as

$$\mathbf{y}_{T:n_t}^{(i+1)} = \mathbf{y}_{T:n_t}^{(i)} + \mu \frac{\partial f}{\partial \mathbf{y}_{T:n_t}}, \quad (46a)$$

$$\mathbf{y}_{R:n_r}^{(i+1)} = \mathbf{y}_{R:n_r}^{(i)} + \mu \frac{\partial f}{\partial \mathbf{y}_{R:n_r}}, \quad (46b)$$

where $\mu > 0$ represents the step size, which is typically obtained via an Armijo line search.

V. PERFORMANCE ANALYSIS

In this section, we analyze both the communications and sensing capabilities of the proposed system, under varying configurations and waveforms⁹. Unless otherwise specified, the fundamental simulation parameters given in Table II persist throughout the section, with important parameters also given in the subtitle of the figures presented. For the mixed term objective of equation (34), we set $\beta = 2$ for a reasonable communication-sensing tradeoff [54].

⁸While the optimization procedure can be executed for each distinct realization of $\bar{\mathbf{H}}(\mathbf{y}_T, \mathbf{y}_R)$ which is a function of $\bar{\mathbf{G}}_p$ and other variables, in practice, after the surface shapes \mathbf{y}_T and \mathbf{y}_R have been computed for a distinct realization, the optimized surface shapes can be used irrespective to changes in delays, Doppler shifts and waveform.

⁹Comparisons against RIS-DD and SIM-DD systems are relegated to future work, since this would require the formulation and solution of similar but independent achievable rate maximization problems.

TABLE II: System Parameters

Parameter	Symbol	Value
Carrier Frequency	f_c	28 GHz
Carrier Wavelength	λ	0.0107 m
System Bandwidth	B	20 MHz
Sampling Frequency	λ	20 MHz
Number of Subcarriers	N	16, 64
Total TX-FIM elements	N_T	4 (2 x 2)
Total RX-FIM elements	N_R	4 (2 x 2)
Total RF chains	d_s	4
Number of Channel Scatterers	P	2, 5
Maximum Range	R_{\max}	120 m
Maximum Velocity	V_{\max}	208 m/s
Maximum Morphing Range	y_{\max}	λ m
Minimum Morphing Range	y_{\min}	$-\lambda$ m

A. Communications Performance

Let us first discuss the communications performance in terms of the achievable rate as portrayed in equation (35). As seen in Figure 2, we present results for OFDM, OTFS and AFDM under the three distinct cases with no FIMs, randomly tuned FIMs and FIMs optimized via the technique described in Algorithm 1. The most fundamental insight gained from these results is that having FIMs at both the TX and the RX significantly improve the achievable rate with a gain of around 2.5 dB going from a case with no FIMs to a case with randomly tuned FIMs. Next, when the FIMs are optimized via Algorithm 1, there is another gain of approximately 2 dB with respect to the case with randomly tuned FIMs.

Notably, the achievable rates for the different waveforms across all the cases are almost identical which is explained by the fact that all three schemes operate within the constraints of the same physical channel, characterized by its bandwidth, noise power, and delay-time channel impulse response.

Performance of OFDM, OTFS and AFDM in terms of Achievable Rate vs. SNR
($N = 64, N_T = N_R = 4, P = 5$)

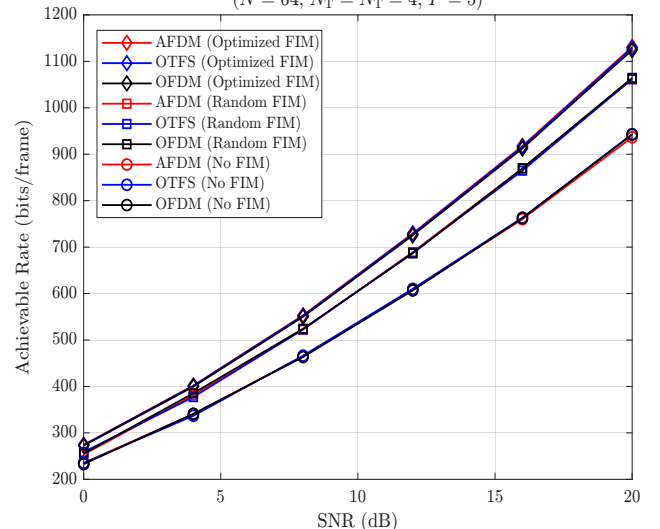


Fig. 2: Achievable Rate vs. signal-to-noise ratio (SNR) of the proposed FIM optimization strategy from Algorithm 1.

Performance of OFDM, OTFS and AFDM in terms of Achievable Rate vs. SNR
($N = 16, N_T = N_R = 4, P = 2$)

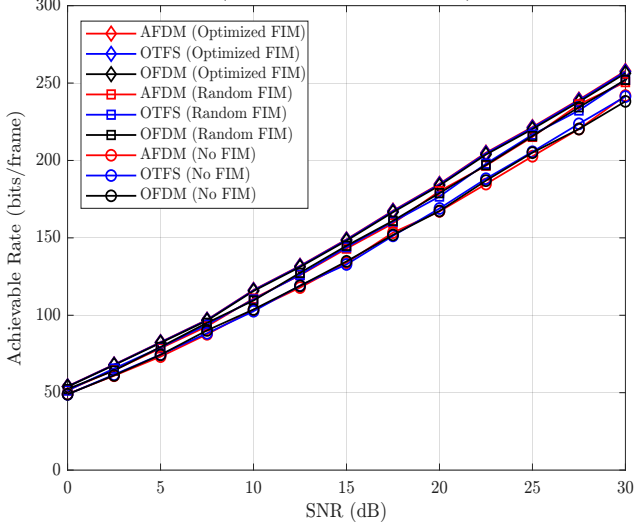


Fig. 3: Achievable Rate vs. SNR of the proposed FIM optimization strategy from Algorithm 1.

Notably, the achievable rates for the different waveforms across all the cases are almost identical which can be explained by the fact that all three schemes operate within the constraints of the same physical channel, characterized by its bandwidth, noise power, and the fundamental delay-time channel impulse response. The achievable rate (or channel capacity), as defined by Shannon's formula, is fundamentally limited by the SNR and bandwidth, regardless of the modulation scheme. However, this result does not translate to practical considerations such as high inter-carrier interference (ICI) which significantly degrade the performance of OFDM compared to OTFS and AFDM as shown in [18].

Next, we analyze the achievable rate for a smaller system size in Figure 3. As seen from the aforementioned figure, there is still a gain with the same trends as seen in Figure 2 when using the FIMs, albeit at a smaller scale due to the lower degrees-of-freedom (DoFs) present.

B. Sensing Performance

After showcasing the performance gains in terms of the achievable rate for communications, let us follow through with a thorough discussion on the sensing capabilities as well. To evaluate the sensing performance, we consider a bistatic¹⁰ setup as seen in Figure 1 where the RX aims to estimate the elevation and azimuth AoAs of all P scatterers with just the knowledge of the received signals \mathbf{y}_{OFDM} , \mathbf{y}_{OTFS} and \mathbf{y}_{AFDM} .

For this purpose, we adopt the well-known Multiple Signal Classification (MUSIC) procedure [53] which is briefly summarized below¹¹. In order to express the MUSIC procedure in a tractable manner for all the waveforms, let us introduce the notation $\bar{\mathbf{y}}$ to denote an arbitrary received signal from any aforementioned modulation procedure.

¹⁰Notice that this setup, like in [55], assumes a blind setting where the RX has no knowledge of the transmit symbols. The procedure for a monostatic scenario is similar with the AoAs being identical to the AoDs. However, this extension is relegated to future work since it requires the addressing of problems such as self-interference [56].

¹¹The MUSIC spectrum can also be directly applied as a constraint in the FIM optimization problem and this setup will be explored in future work.

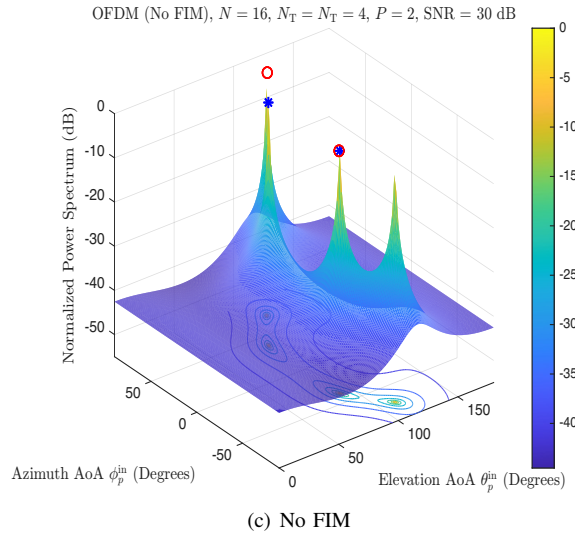
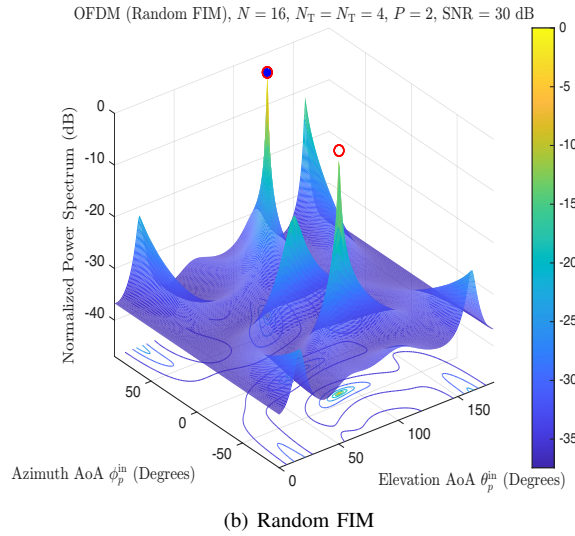
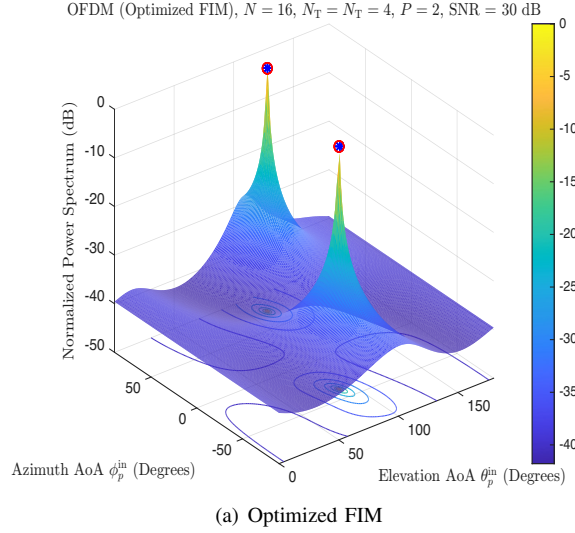


Fig. 4: Normalized Power Spectrum for OFDM waveforms obtained via the MUSIC algorithm at the RX side with $P = 2$. The red circles on each figure represents the true location of each p -th scatterer, while the blue stars represent the estimated positions of each p -th scatterer via the MUSIC algorithm.

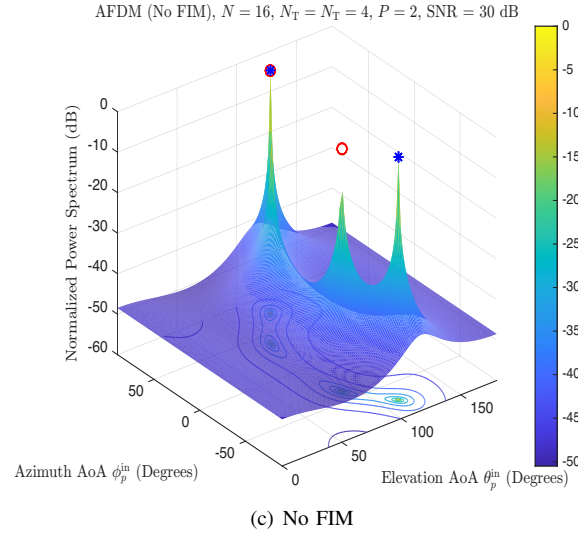
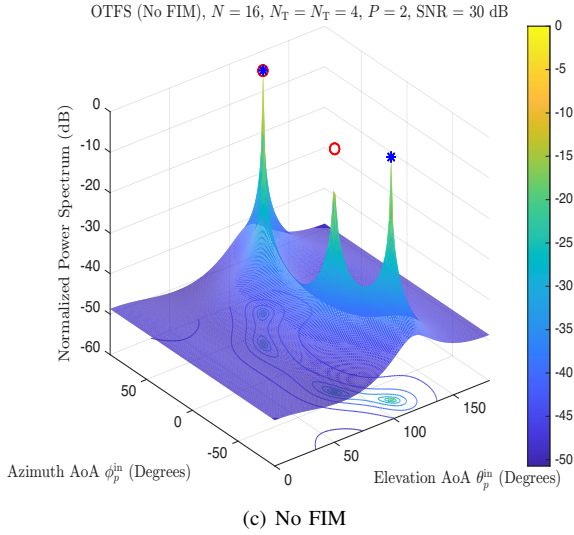
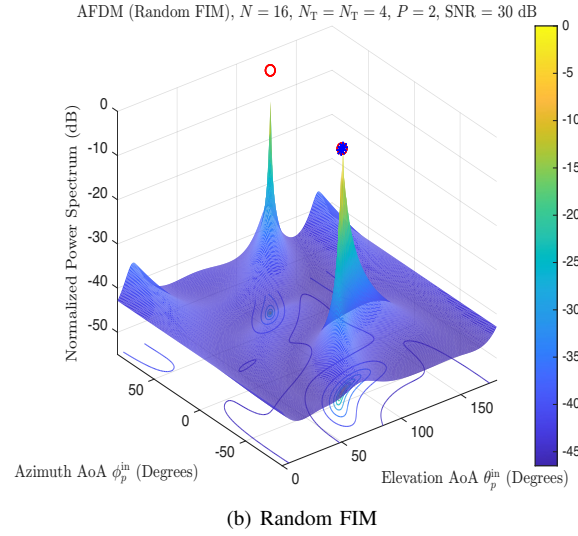
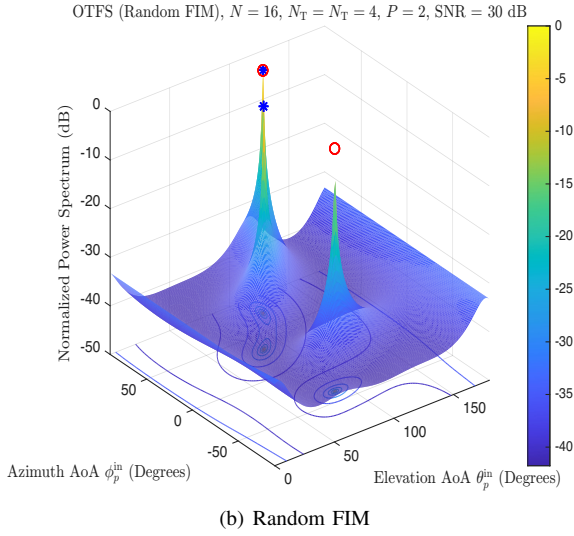
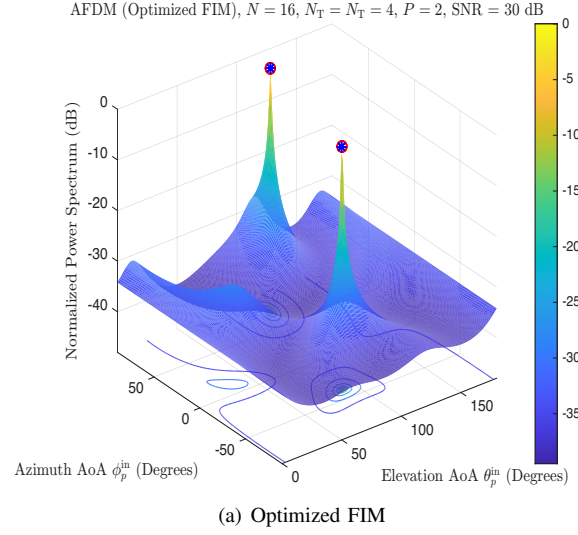
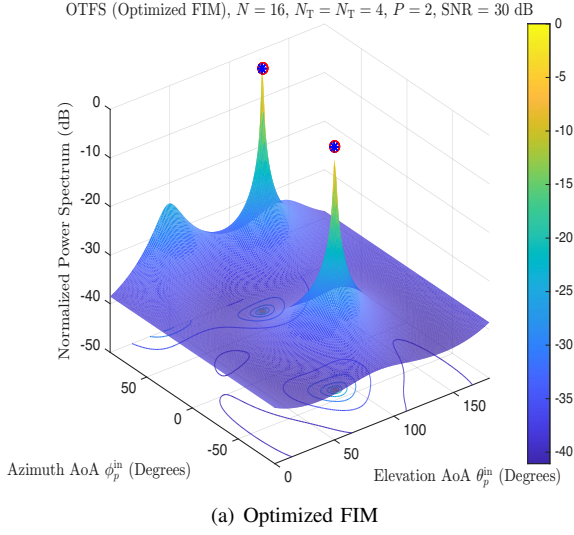


Fig. 5: Normalized Power Spectrum for OTFS waveforms obtained via the MUSIC algorithm at the RX side with $P = 2$. The red circles on each figure represents the true location of each p -th scatterer, while the blue stars represent the estimated positions of each p -th scatterer via the MUSIC algorithm.

Fig. 6: Normalized Power Spectrum for AFDM waveforms obtained via the MUSIC algorithm at the RX side with $P = 2$. The red circles on each figure represents the true location of each p -th scatterer, while the blue stars represent the estimated positions of each p -th scatterer via the MUSIC algorithm.

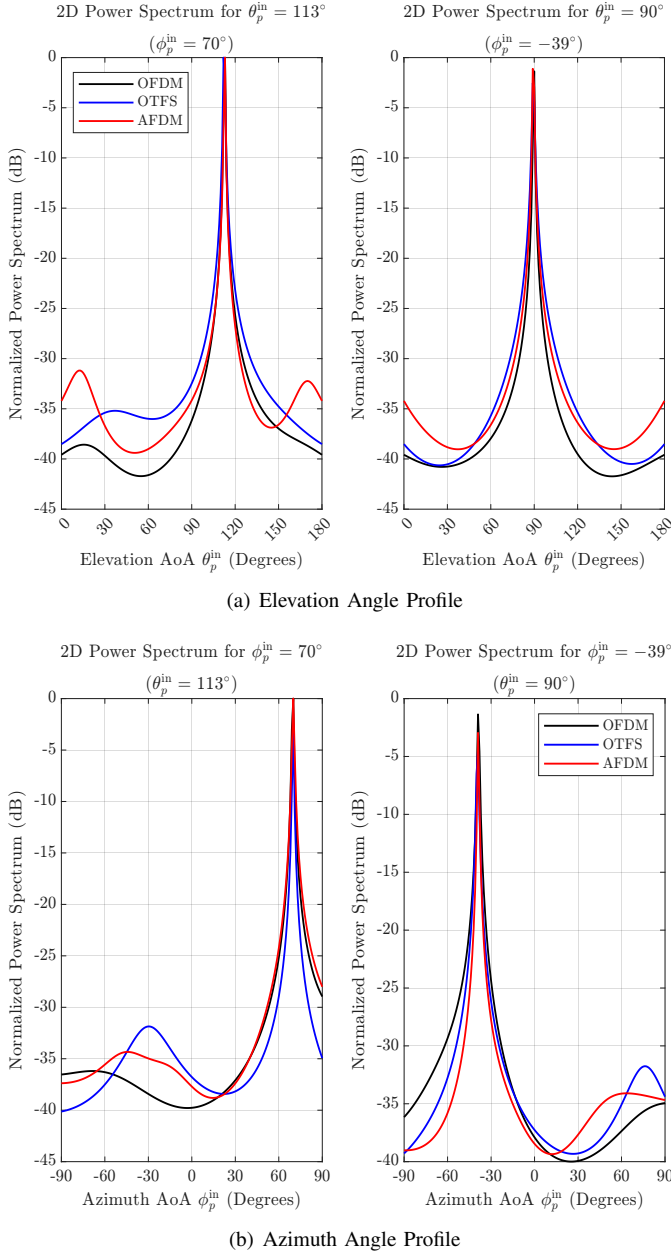


Fig. 7: Normalized 2D Power Spectrum for different waveforms obtained via the MUSIC algorithm at the RX side with $P = 2$.

The received signal $\bar{\mathbf{y}}$ is first preprocessed via a vector inverse operation

$$\bar{\mathbf{Y}} = \text{vec}^{-1}(\bar{\mathbf{y}})^H \in \mathbb{C}^{d_s \times N}, \quad (47)$$

where the $\text{vec}^{-1}(\cdot)$ denotes a column-wise unstacking such that the $Nd_s \times 1$ vector is shaped into a $N \times d_s$ matrix.

Next, the RX covariance matrix $\mathbf{R}_{\bar{\mathbf{y}}}$ can be computed as

$$\mathbf{R}_{\bar{\mathbf{y}}} = \bar{\mathbf{Y}}\bar{\mathbf{Y}}^H \in \mathbb{C}^{d_s \times d_s}. \quad (48)$$

Denoting $\bar{\mathbf{U}} \in \mathbb{C}^{d_s \times d_s}$ to be the set of ascending eigenvectors of $\mathbf{R}_{\bar{\mathbf{y}}}$, the eigenvectors corresponding to the noise subspace of the P scatterers can be extracted as $\bar{\mathbf{U}}_N \triangleq \bar{\mathbf{U}}[:, d_s - P] \in \mathbb{C}^{d_s \times P}$, which chooses the first P columns of $\bar{\mathbf{U}}$.

Finally, the 2D MUSIC spectrum for a given angle pair $(\phi_p^{\text{in}}, \theta_p^{\text{in}})$ can be expressed as

$$M(\phi_p^{\text{in}}, \theta_p^{\text{in}}) = \frac{1}{\mathbf{b}_{\text{R}:p}^H(\mathbf{y}_{\text{R}}^*, \phi_p^{\text{in}}, \theta_p^{\text{in}}) \bar{\mathbf{U}}_N \bar{\mathbf{U}}_N^H \mathbf{b}_{\text{R}:p}(\mathbf{y}_{\text{R}}^*, \phi_p^{\text{in}}, \theta_p^{\text{in}})}, \quad (49)$$

where we re-emphasize that $\mathbf{b}_{\text{R}:p}(\mathbf{y}_{\text{R}}^*, \phi_p^{\text{in}}, \theta_p^{\text{in}})$ is the RX-FIM response vector computed at each pair $(\phi_p^{\text{in}}, \theta_p^{\text{in}})$ alongside the optimal solution \mathbf{y}_{R}^* .

Figures 4, 5 and 6 now present results for the OFDM, OTFS and AFDM waveforms respectively, in the cases where no FIMs is present, randomly tuned FIMs are present and FIMs optimized via the technique described in Algorithm 1 are present. As seen in common across all the waveforms, in the presence of optimized FIMs, the 2D MUSIC spectrum clearly identifies the elevation and azimuth AoA of each scatterer with strong peaks while with randomly tuned FIMs, 2D MUSIC yields some peaks but fails to correctly isolate the scatterers. In addition, when there are no FIMs present, there are multiple distinct peaks that do not correspond to the actual scatterer locations and hence, the positions are not identified correctly.

Finally, to compare the performances of distinct waveforms, Figure 7 offers cuts parallel to both the elevation and azimuth directions of the 2D spectra for both scatterers. As seen from Figure 7(a), while the power of the peaks are similar across all three waveforms, OFDM has the lowest sidelobes for the best isolation of the peaks, with OTFS and AFDM not far behind. Figure 7(b) also shows a similar scenario where OFDM seems to have the lowest sidelobes albeit not by a large margin.

VI. CONCLUSION

We proposed a FIM-based ISAC DD MIMO channel model that proves highly effective for high-mobility scenarios. We then formulated and solved an achievable rate maximization problem with a stringent sensing constraint using a gradient ascent algorithm, supplemented by closed-form gradients, which are shown to yield significant performance gains for the key ISAC waveforms, namely, OFDM, OTFS, and AFDM. Numerical results underscore the critical role of FIM technology, highlighting that precise parametrization is essential for optimizing ISAC performance across all evaluated waveforms, effectively mitigating the challenges of DD channels. An exciting possibility, to be explored in future work, is to consider the impact of FIM on the angular resolution of AoA/AoD estimation, which is a key aspect of ISAC systems.

REFERENCES

- [1] N. C. Luong *et al.*, “Advanced learning algorithms for integrated sensing and communication (ISAC) systems in 6G and beyond: A comprehensive survey,” *IEEE Communications Surveys & Tutorials*, pp. 1–1, 2025.
- [2] K. R. R. Ranasinghe, K. Ando, and G. T. Freitas de Abreu, “From theory to reality: A design framework for integrated communication and computing receivers,” in *2025 International Conference on Computing, Networking and Communications (ICNC)*, 2025, pp. 865–870.
- [3] K. R. R. Ranasinghe, K. Ando, H. S. Rou, G. T. F. de Abreu, T. Takahashi, M. D. Renzo, and D. G. Gonzalez, “A flexible design framework for integrated communication and computing receivers,” 2025. [Online]. Available: <https://arxiv.org/abs/2506.05944>
- [4] H. Yu, M. Shokrnezhad, T. Taleb, R. Li, and J. Song, “Toward 6G-based metaverse: Supporting highly-dynamic deterministic multi-user extended reality services,” *IEEE Network*, vol. 37, no. 4, pp. 30–38, 2023.

- [5] V.-D. Nguyen *et al.*, "Network-aided intelligent traffic steering in 6G O-RAN: A multi-layer optimization framework," *IEEE Journal on Selected Areas in Communications*, vol. 42, no. 2, pp. 389–405, 2024.
- [6] H. Cui *et al.*, "Space-air-ground integrated network (SAGIN) for 6G: Requirements, architecture and challenges," *China Communications*, vol. 19, no. 2, pp. 90–108, 2022.
- [7] R. Deng *et al.*, "Reconfigurable holographic surfaces for ultra-massive MIMO in 6G: Practical design, optimization and implementation," *IEEE Journal on Selected Areas in Comm.*, vol. 41, no. 8, 2023.
- [8] M. Z. Chowdhury *et al.*, "6G wireless communication systems: Applications, requirements, technologies, challenges, and research directions," *IEEE Open Journal of the Communications Society*, vol. 1, 2020.
- [9] S. Dang, O. Amin, B. Shihada, and M.-S. Alouini, "What should 6G be?" *Nature Electronics*, vol. 3, no. 1, pp. 20–29, 2020.
- [10] M. Giordani, M. Polesse, M. Mezzavilla, S. Rangan, and M. Zorzi, "Toward 6G networks: Use cases and technologies," *IEEE Communications Magazine*, vol. 58, no. 3, pp. 55–61, 2020.
- [11] D. W. Bliss and S. Govindasamy. Cambridge University Press, 2013.
- [12] F. Tariq *et al.*, "A speculative study on 6G," *IEEE Wireless Communications*, vol. 27, no. 4, pp. 118–125, 2020.
- [13] H. S. Rou *et al.*, "From orthogonal time–frequency space to affine frequency-division multiplexing: A comparative study of next-generation waveforms for integrated sensing and communications in doubly dispersive channels," *IEEE Signal Process. Mag.*, vol. 41, no. 5, 2024.
- [14] R. Hadani *et al.*, "Orthogonal time frequency space modulation," in *Proc. IEEE WCNC*, San Francisco, USA, 2017.
- [15] F. Liu *et al.*, "Integrated sensing and communications: Toward dual-functional wireless networks for 6G and beyond," *IEEE Journal on Selected Areas in Comm.*, vol. 40, no. 6, pp. 1728–1767, 2022.
- [16] N. T. Nguyen *et al.*, "Joint communications and sensing hybrid beamforming design via deep unfolding," *IEEE Journal of Selected Topics in Signal Processing*, vol. 18, no. 5, pp. 901–916, 2024.
- [17] Z. Xiao *et al.*, "A novel joint angle-range-velocity estimation method for MIMO-OFDM ISAC systems," *IEEE Transactions on Signal Processing*, vol. 72, pp. 3805–3818, 2024.
- [18] K. R. R. Ranasinghe *et al.*, "Joint channel, data, and radar parameter estimation for AFDM systems in doubly-dispersive channels," *IEEE Transactions on Wireless Communications*, vol. 24, no. 2, 2025.
- [19] Y. Luo *et al.*, "A novel angle-delay-doppler estimation scheme for AFDM-ISAC system in mixed near-field and far-field scenarios," *IEEE Internet of Things Journal*, vol. 12, no. 13, 2025.
- [20] X. Cheng, D. Duan, S. Gao, and L. Yang, "Integrated sensing and communications (ISAC) for vehicular communication networks (VCN)," *IEEE Internet of Things Journal*, vol. 9, no. 23, pp. 23 441–23 451, 2022.
- [21] G. C. Alexandropoulos *et al.*, "Hybrid reconfigurable intelligent metasurfaces: Enabling simultaneous tunable reflections and sensing for 6G wireless communications," *IEEE Vehicular Technology Magazine*, vol. 19, no. 1, pp. 75–84, 2024.
- [22] A. Stutz-Tirri *et al.*, "Efficient and physically consistent modeling of reconfigurable electromagnetic structures," *IEEE Open Journal of the Communications Society*, vol. 6, pp. 1610–1633, 2025.
- [23] D. Dardari, "Over-the-air multifunctional wideband electromagnetic signal processing using dynamic scattering arrays," 2025. [Online]. Available: <https://arxiv.org/abs/2506.00619>
- [24] V. G. Ataloglou and G. V. Eleftheriades, "A reconfigurable intelligent surface with surface-wave assisted beamforming capabilities," *IEEE Transactions on Antennas and Propagation*, pp. 1–1, 2025.
- [25] T. J. Cui *et al.*, "Coding metamaterials, digital metamaterials and programmable metamaterials," *Light Sci. & Appl.*, vol. 3, no. 10, 2014.
- [26] N. Kolomvakis, A. Kosasih, and E. Björnson, "Nonlinear distortion radiated from large arrays and active reconfigurable intelligent surfaces," *IEEE Transactions on Wireless Communications*, vol. 24, no. 6, 2025.
- [27] S. Droulias, G. Stratidakis, E. Björnson, and A. Alexiou, "Reconfigurable intelligent surfaces as spatial filters," *IEEE Transactions on Wireless Communications*, vol. 23, no. 11, pp. 16 922–16 934, 2024.
- [28] X. Zhang, H. Zhang, L. Liu, Z. Han, H. V. Poor, and B. Di, "Target detection and positioning aided by reconfigurable surfaces: Reflective or holographic?" *IEEE Transactions on Wireless Communications*, vol. 23, no. 12, pp. 19 215–19 230, 2024.
- [29] J. An *et al.*, "Stacked intelligent metasurface-aided MIMO transceiver design," *IEEE Wireless Commun.*, vol. 31, no. 4, pp. 123–131, 2024.
- [30] J. An *et al.*, "Stacked intelligent metasurfaces for efficient holographic MIMO communications in 6G," *IEEE J. Sel. Areas Commun.*, vol. 41, no. 8, pp. 2380–2396, 2023.
- [31] J. An *et al.*, "Flexible intelligent metasurfaces for downlink multiuser MISO communications," *IEEE Trans. Wireless Commun.*, vol. 24, no. 4, pp. 2940–2955, 2025.
- [32] Y. Bai *et al.*, "A dynamically reprogrammable surface with self-evolving shape morphing," *Nature*, vol. 609, no. 7928, pp. 701–708, Sep. 2022.
- [33] J. An, M. Debbah, T. J. Cui, Z. N. Chen, and C. Yuen, "Emerging technologies in intelligent metasurfaces: Shaping the future of wireless communications," *IEEE Trans. Antennas Propag.*, pp. 1–1, 2025.
- [34] X. Ni *et al.*, "An ultrathin invisibility skin cloak for visible light," *Sci.*, vol. 349, no. 6254, pp. 1310–1314, Sep. 2015.
- [35] S. M. Kamali *et al.*, "Decoupling optical function and geometrical form using conformal flexible dielectric metasurfaces," *Nature Commun.*, vol. 7, no. 1, p. 11618, May 2016.
- [36] X. Ni *et al.*, "Soft shape-programmable surfaces by fast electromagnetic actuation of liquid metal networks," *Nature Commun.*, vol. 13, no. 1, p. 5576, Sep. 2022.
- [37] J. An *et al.*, "Flexible intelligent metasurfaces for enhancing MIMO communications," *IEEE Trans. Commun.*, pp. 1–15, 2025, Early Access.
- [38] Z. Teng *et al.*, "Flexible intelligent metasurface for enhancing multi-target wireless sensing," *IEEE Trans. Veh. Technol.*, pp. 1–6, 2025.
- [39] K. R. R. Ranasinghe *et al.*, "Metasurfaces-integrated doubly-dispersive MIMO: Channel modeling and optimization," 2025. [Online]. Available: <https://arxiv.org/abs/2506.14985>
- [40] K. R. R. Ranasinghe *et al.*, "Doubly-dispersive MIMO channels with stacked intelligent metasurfaces: Modeling, parametrization, and receiver design," 2025. [Online]. Available: <https://arxiv.org/abs/2501.07724>
- [41] K. R. R. Ranasinghe, I. A. M. Sandoval, G. T. F. de Abreu, and G. C. Alexandropoulos, "Parametrized stacked intelligent metasurfaces for bistatic integrated sensing and communications," 2025. [Online]. Available: <https://arxiv.org/abs/2504.20661>
- [42] J. An *et al.*, "Stacked intelligent metasurfaces for efficient holographic MIMO communications in 6G," *IEEE J. Sel. Areas Commun.*, vol. 41, no. 8, pp. 2380–2396, 2023.
- [43] J. An, C. Yuen *et al.*, "Flexible intelligent metasurfaces for downlink multiuser miso communications," *IEEE Transactions on Wireless Communications*, pp. 1–1, 2025.
- [44] J. An *et al.*, "Two-dimensional direction-of-arrival estimation using stacked intelligent metasurfaces," *IEEE J. Sel. Areas Commun.*, vol. 42, no. 10, pp. 2786–2802, 2024.
- [45] S. Srivastava, R. K. Singh, A. K. Jagannatham, A. Chockalingam, and L. Hanzo, "Otf's transceiver design and sparse doubly-selective csi estimation in analog and hybrid beamforming aided mmwave mimo systems," *IEEE Transactions on Wireless Communications*, vol. 21, no. 12, pp. 10 902–10 917, 2022.
- [46] Y. Yan, C. Shan, J. Zhang, and H. Zhao, "Off-grid channel estimation for OTFS-based mmwave hybrid beamforming systems," *IEEE Commun. Lett.*, vol. 27, no. 8, pp. 2167–2171, 2023.
- [47] K. R. R. Ranasinghe, Y. Ge, G. T. Freitas de Abreu, and Y. Liang Guan, "Joint channel estimation and sparse detection for AFDM receivers with oversampling," in *Proc. International Conference on Computing, Networking and Communications (ICNC)*, 2025.
- [48] P. Raviteja *et al.*, "Interference cancellation and iterative detection for orthogonal time frequency space modulation," *IEEE Trans. Wireless Commun.*, vol. 17, no. 10, 2018.
- [49] A. Bemani, N. Ksairi, and M. Kountouris, "Affine frequency division multiplexing for next generation wireless communications," *IEEE Trans. Wireless Commun.*, vol. 22, no. 11, pp. 8214–8229, 2023.
- [50] J. Zhu, Y. Tang, X. Wei, H. Yin, J. Du, Z. Wang, and Y. Liu, "A low-complexity radar system based on affine frequency division multiplexing modulation," *arXiv preprint arXiv:2312.11125*, 2023.
- [51] G. Liu, T. Mao, R. Liu, and Z. Xiao, "Pre-chirp-domain index modulation for affine frequency division multiplexing," *arXiv preprint arXiv:2402.15185*, 2024.
- [52] H. S. Rou *et al.*, "AFDM chirp-permutation-index modulation with quantum-accelerated codebook design," *IEEE Proceedings of the Asilomar Conference on Signals, Systems and Computers (ASILOMAR)* 2024. [Online]. Available: <https://arxiv.org/abs/2405.02085>
- [53] K. R. R. Ranasinghe, H. S. Rou, and G. T. F. de Abreu, "Fast and efficient sequential radar parameter estimation in MIMO-OTFS systems," in *Proc. IEEE ICASSP*, Seoul, South Korea, 2024.
- [54] H. Niu, J. An, A. Papazafeiropoulos, L. Gan, S. Chatzinotas, and M. Debbah, "Stacked intelligent metasurfaces for integrated sensing and communications," *IEEE Wireless Communications Letters*, 2024.
- [55] K. R. R. Ranasinghe *et al.*, "Blind bistatic radar parameter estimation for AFDM systems in doubly-dispersive channels," in *Proc. IEEE Wireless Communications and Networking Conference (WCNC)*, 2024. [Online]. Available: <https://arxiv.org/abs/2407.05328>
- [56] A. Bemani, N. Ksairi, and M. Kountouris, "Integrated sensing and communications with affine frequency division multiplexing," *IEEE Wireless Commun. Lett.*, early access, 2024.